Supple Formamidinium-Based Low-Dimension Perovskite Derivative for Sensitive and Ultrastable X-ray Detection

Zihan Wang, Shujie Tie, Hui Zhang, Wan Changmao, Zheng Liang, Huifen Xu, Xiaojia Zheng, Wenhua Zhang, Dmitry Aldakov, Peter Reiss, et al.

▶ **To cite this version:**

Zihan Wang, Shujie Tie, Hui Zhang, Wan Changmao, Zheng Liang, et al.. Supple Formamidinium-Based Low-Dimension Perovskite Derivative for Sensitive and Ultrastable X-ray Detection. ACS Nano, 2023, 17 (14), pp.13638-13647. 10.1021/acsnano.3c02476 . hal-04191047

HAL Id: hal-04191047

https://cnrs.hal.science/hal-04191047v1

Submitted on 15 Nov 2023

HAL is a multi-disciplinary open access archive for the deposit and dissemination of scientific research documents, whether they are published or not. The documents may come from teaching and research institutions in France or abroad, or from public or private research centers.

L'archive ouverte pluridisciplinaire **HAL**, est destinée au dépôt et à la diffusion de documents scientifiques de niveau recherche, publiés ou non, émanant des établissements d'enseignement et de recherche français ou étrangers, des laboratoires publics ou privés.

Suppleness formamidinium-based low-dimension perovskite derivative for sensitive and ultrastable X-Ray detection

Zihan Wang [1,2#], Shujie Tie[3#], Hui Zhang [1], Wan Changmao[1], Zheng Liang[1], Huifen Xu[1], Xiaojia Zheng[3], Wenhua Zhang[4], Dmitry Aldakov[5], Peter Reiss,[5] Jiajiu YE,[1,6]* Xu Pan[1]**

1. Institute of Solid-State Physics, Hefei Institutes of Physical Science, Chinese Academy of Science, Hefei 230031, China.

2. University of Science and Technology of China, Hefei 230026, China.

3. Sichuan Research Center of New Materials, Institute of Chemical Materials, China Academy of Engineering Physics, Chengdu 610200, Sichuan, China.

4. School of Materials and Energy, Yunnan University, Kunming 650091, China.

5. Univ. Grenoble Alpes, CEA, CNRS, INP, IRIG/SyMMES, STEP, 38000 Grenoble, France.

6. IEK5-Photovoltaics, Forschungszentrum Jülich, 52425 Jülich, Germany.

# contributed equally to this work

Corresponding Authors: xiaojia@caep.cn, yejj@issp.ac.cn, xpan@rntek.cas.cn

Keywords: Yellow Phase $FAPbI_3$, Suppleness Perovskite Materials, Perovskite Wafer, Stable X-ray detector, X-ray imaging.

Abstract

Halide perovskite materials possess remarkable optoelectronic properties and have shown great potential for direct X-ray detection. Perovskite wafers are particularly attractive among various detection structures due to their scalability and ease of preparation, making them the most promising candidate for X-ray detection and array imaging applications. However, device instability and current drift caused by ionic migration is a persistent challenge for perovskite detectors, especially in polycrystalline wafers with numerous grain boundaries. In this study, we examined the potential of one-dimensional (1D) δ-phase (yellow phase) formamidinium lead iodide (δ-$FAPbI_3$) as an X-ray detection material. This material possesses a suitable band gap of 2.42 eV, which makes it highly promising for X-ray detection and imaging using compact wafers. Moreover, we found that δ-$FAPbI_3$ has low ionic migration, low Young's modulus, and excellent long-term stability, making it an ideal candidate for high-performance X-ray detection. Notably, the yellow phase perovskite derivative exhibit exceptional long-term atmospheric stability (RH of ≈70±5%) over six months, as well as an extremely low dark current drift (3.43×10^{-4} pA cm^{-1} s^{-1} V^{-1}), which is comparable to that of single crystal devices. An X-ray imager with a large size δ-$FAPbI_3$ wafer integrated on thin film transistor (TFT) backplane was further fabricated. Direct 2D multi-pixel radiographic imaging was successfully performed, demonstrating the feasibility of δ-$FAPbI_3$ wafer detectors for sensitive and ultra-stable imaging applications.

Introduction

Halide perovskites are considered one of the most promising materials for commercial direct X-ray detection due to their high X-ray conversion efficiency, large attenuation coefficient to X-ray source, high spatial resolution imaging, and great mobility-lifetime product (μτ).[1-3] Compared to commonly used materials such as CdZnTe (CZT), CsI, and a-Se, perovskite detectors exhibit several orders of magnitude higher sensitivity, superior detection limits, and much better resolution. These properties make perovskite

detectors ideal for mechanical diagnosis, security screening, and other fields.[4-6] A satisfactory perovskite X-ray detector is typically characterized by several essential properties, including adequate thickness to ensure efficient X-ray absorption, excellent optoelectronic properties for high sensitivity detection, and high stability in the operating environment. Furthermore, for commercial flat imaging applications, the perovskite detectors must possess scalability that are sufficiently large to match the size of the object under inspection.[7-9]

However, it is currently challenging to produce millimeter-thick large-area films using traditional deposition techniques or blade coating. On the other hand, the production of perovskite single crystal detectors is restricted by immature technology and high costs, particularly for the low-dimensional perovskite crystals.[10, 11] Due to its highly tunable nature and cost-effective production processes, the fabrication of perovskite wafers represents a simple and commercially viable approach for developing X-ray detectors.[12] This method can be easily scaled up using molds or patterns, making it preferable to single crystals. The properties of perovskite wafer devices endow them with high competitiveness for commercial products and applications. Shrestha et al. first reported a room-temperature sintering process to fabricate thick $MAPbI_3$ wafer with a sensitivity of 2,527 μC Gy_{air}^{-1} cm^{-2}.[13] Tie et al. have published findings on the operational stability and high sensitivity of (0D) $MA_3Bi_2I_9$ polycrystalline pellets.[14] Similarly, Tang et al. fabricated a pinhole-free and high-performance $Cs_2AgBiBr_6$ wafer using the hot-pressing method as well.[15] Previous studies have demonstrated the successful fabrication of thick perovskite wafers with remarkably high sensitivity, surpassing that of commercial α-Se detectors, and validating the practicality of them for X-ray detection.

However, a significant challenge facing the development of perovskite detectors is the uncontrollable migration of ions, high dark carrier concentration, and phase separation observed. The emergence of numerous cracks and voids porosities in the wafers leads to more severe ion migration, accelerates the decomposition of perovskite, and interferes with the signal collection, potentially hindering the growth of perovskite

detectors and cancelling their potential advantages.[16-18] Moreover, despite their advantageous optoelectronic properties, traditional 3D hybrid perovskite single crystals, and wafers are still dominated by unstable methylammonium (MA) and formamidinium (FA) A-site cations. The propensity for these cations to decompose or undergo phase separation in 3D hybrid perovskites leads to device stability issues, thereby impeding the long-term reliability of perovskite-based devices.[19-21]

In this study, a high-performance perovskite derivative X-ray detector with excellent stability was developed. Specifically, a highly compact wafer for X-ray detection was fabricated using 1D δ-$FAPbI_3$ (yellow phase) for the first time. The low-dimensional structure of the δ-$FAPbI_3$ results in a high activation energy (E_a) for ion migration, which naturally offers high stability. The δ-$FAPbI_3$ precursor powders exhibit low Young's modulus and high internal homogeneity, Consequently, the wafers obtained by the cold isostatic pressing method have low porosity, low residual stress and fewer defect. This, in turn, effectively limits ion migration and improves charge transport properties. As a result, the wafer detector device exhibits a high sensitivity of 590.6 μC Gy_{air}^{-1} cm^{-2} under 50 kV X-ray, excellent long-term stability of 6 months under ambient atmosphere, and an ultralow dark current drift of 3.43×10^{-4} pA cm^{-1} s^{-1} V^{-1}. Notably, we demonstrated that the δ-$FAPbI_3$ wafers could be integrated with TFT readout arrays and realized direct 2D multipixel X-ray imaging.

Results and discussions

δ-$FAPbI_3$ precursor powders for wafers

Polycrystalline powders of δ-$FAPbI_3$ were fabricated by the wet-chemical reaction of FAI and PbI_2 at room temperature. As illustrated in Fig. 1a, with the surface-active sites of PbI_2 and FAI particles continuously colliding and initiating further chemical reactions, δ-$FAPbI_3$ polycrystals can be obtained. Scanning electron microscopy (SEM) shows that the synthesized yellow δ-$FAPbI_3$ powders have a rod-shaped blocks structure with a wide distribution of particles sizes from 1 to 70 μm (Fig. 1b, S1). The energy dispersive spectroscopy (EDS) mapping profile for a single block demonstrated

the uniform distribution of C, N, I and Pb elements (Fig. S2). The tail of the rod structure was cracked into ultra-fine single crystals under the effect of prolonged ultrasound (Fig. 1c, Fig. S3), and HRTEM revealed clear lattice fringes with interplanar spacing of 0.271 nm along the long axis, which matches with the (022) lattice spacing of δ-$FAPbI_3$ (Fig. 1d).[22]

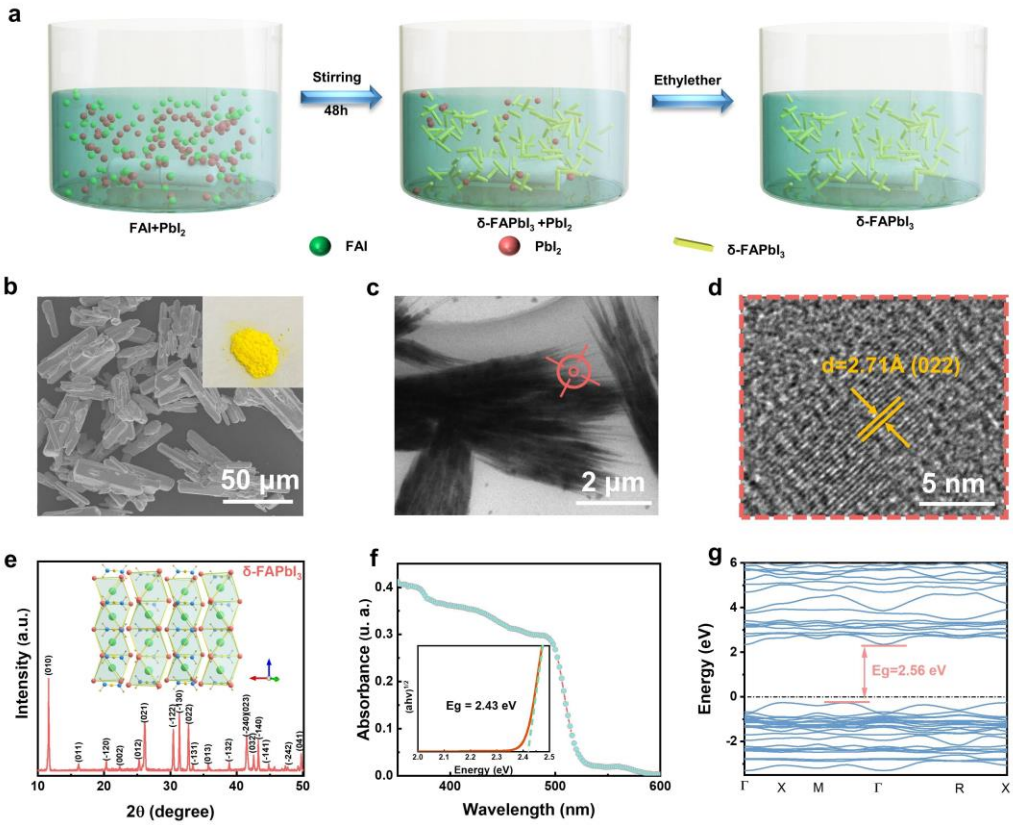

Figure 1. Fabrication and characterization of 1D δ-$FAPbI_3$ polycrystalline powders. (a) Schematic of δ-$FAPbI_3$ polycrystalline powders synthesized processing. (b) SEM and optical(inset) images of δ-$FAPbI_3$ polycrystalline powders, (c) TEM and (d) HRTEM images of δ-$FAPbI_3$ polycrystalline powders. (e) XRD pattern of δ-$FAPbI_3$ polycrystalline powders and its crystal structure (inset); (f) Absorption spectrum of δ-$FAPbI_3$ with its Tauc plot (inset) (g) Calculated electronic band structure of δ-$FAPbI_3$.

To investigate the structural properties of the powders, X-ray diffraction measurements were performed. As shown in Fig. 1e, the diffraction peaks of δ-$FAPbI_3$

powders at 11.6°, 26.2°, 30.5°, 31.4° and 32.7° are related to the lattice planes (010), (021), (-122), (-130) and (022), respectively, which fits well with the hexagonal system ($P6_3mc$ space group) with unit-cell parameters of a = b = 8.6603 Å and c =7.9022 Å.[23, 24] It demonstrated that pure δ-phase $FAPbI_3$ powders were obtained without PbI_2 residues. The inset illustration presents the δ-$FAPbI_3$ structure with face-sharing octahedra growing along the (001) direction to form single chains.[25] The FA^+ cation occupies the space between the chains, resulting in a 1D crystal structure and presenting the potential for suppressing ion migration. Optical absorption spectra of δ-$FAPbI_3$ powders shows the absorption edge at approximately 520 nm, demonstrating a suitable optical band gap of 2.43 eV for an X-ray detector (Fig. 1f).[10, 26] DFT calculations were further conducted to the evaluate electronic band structure of δ-$FAPbI_3$. The band gap of frontier molecular orbital was revealed by projected density of states (PDOS). Fig. S4 showed that the valence band maximum (VBM) of the δ-$FAPbI_3$ is mainly constituted of I 5p and Pb 6s contributions, and the conduction band minimum (CBM) is dominated by Pb 6p. Overall, the electronic band structure (Fig. 1g) shows that δ-$FAPbI_3$ is an indirect band gap semiconductor with a band gap of 2.56 eV. The bandgap discrepancy between experimental and theoretical calculations is mainly owing to a strong spin-orbit coupling (SOC) effects introduced by heavy Pb constituent[27].

Structural and mechanical investigations

To compare with the widely used cubic black phase $FAPbI_3$ (α-$FAPbI_3$)[28], α-$FAPbI_3$ polycrystalline particles with an average diameter of 0.5-8 μm were also prepared (Fig. S5, 6). Because of the one-dimensional hollow tube structure of δ-$FAPbI_3$ SCs (Fig. S7), it is obviously difficult to make the required detector based on these small fragile SCs, let alone orderly assemble these onto large flat-panel arrays for imaging. Here, cold isostatic-pressing technique was adopted to fabricate millimeter-thick $FAPbI_3$ wafers.[14] Fig. 2a illustrates the fabrication procedure. The pre-prepared powders were compacted at a pressure of 0.2 G Pa for 10 min, and then the two wafers were got as shown in Fig.

S8. Interestingly, the α-$FAPbI_3$ wafer exhibits the same black color as the precursor powder, while the δ-$FAPbI_3$ wafer has an orange-red color rather than the yellow one of the precursor powders. This color change is mainly due to the piezochromism property of δ-$FAPbI_3$.[29] The pressure-induced the optical absorption spectra of δ-$FAPbI_3$ slightly red-shifted, and the corresponding band gap decreases from 2.43 eV for precursor powders to 2.38 eV for δ-$FAPbI_3$ wafer (Fig. S9). Meanwhile, the XRD pattern of both wafers showed the same characteristic peaks as for the precursor powders (Fig. S10), demonstrating that both phases maintain their original crystallized phase after cold isostatic-pressing treatment.

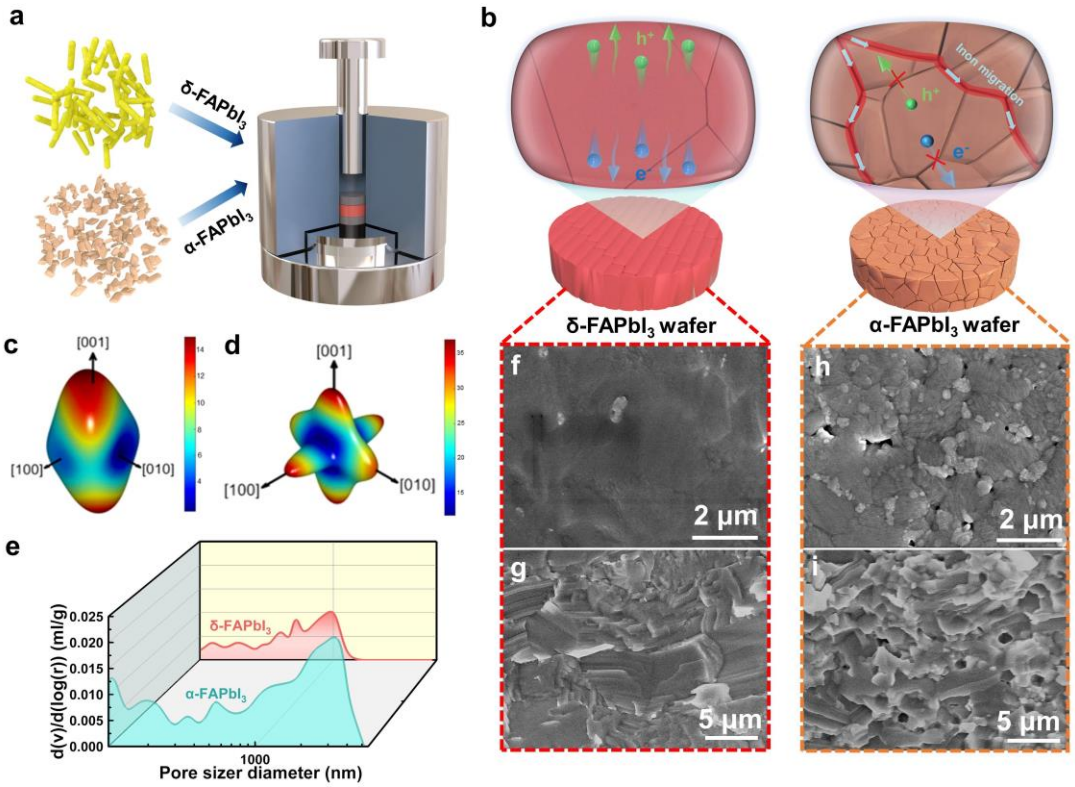

Figure 2. Preparation and characterization of δ-$FAPbI_3$ and α-$FAPbI_3$ wafers (a) Cold isostatic-pressing method to fabricate δ-$FAPbI_3$ and α-$FAPbI_3$ wafers. (b) Schematic illustration for the structure of δ-$FAPbI_3$ and α-$FAPbI_3$ wafers. (c) Surfaces of Young's modulus of the δ-$FAPbI_3$ and (d) α-$FAPbI_3$. (e) Differential pore size distribution of the δ-$FAPbI_3$ and α-$FAPbI_3$ wafers measured

by MIP; (f) Top view and (g) cross-sectional SEM images of the δ-$FAPbI_3$ wafers; (h) Top view and (i) cross-sectional SEM images of the α-$FAPbI_3$ wafers.

Fig. 2c, d shows the value of Young's modulus of the δ-$FAPbI_3$ and α-$FAPbI_3$ precursor powders, evaluated within Voigt–Reuss–Hill (VRH) approximation via DFT calculations.[30, 31] Table S1 shows that the modulus along all directions of δ-$FAPbI_3$ crystal (7.93-4.49 GPa) is significantly smaller than that of the α-$FAPbI_3$ (23.91-17.70 GPa). This discrepancy could be attributed to the lower interchain stiffness and structural symmetry of hexagonal phase δ-$FAPbI_3$ than that of the 3D framework of cubic phase α-$FAPbI_3$.[30, 32] Meanwhile, we also performed the nanoindentation measurement on the δ-$FAPbI_3$ and α-$FAPbI_3$ wafers (Fig. S11). The results show that the Young's modulus and hardness of δ-$FAPbI_3$ is 6.01 G Pa and 0.21 G Pa, respectively. The α-$FAPbI_3$ have a higher Young's modulus for 13.89 G Pa and hardness for 0.48 G Pa, which is in a good agreement with DFT calculation result. The mechanical properties of $FAPbI_3$ determine the deformation response to external pressure, and further influences on the interparticle binding area and binding strength. It shows that that δ-$FAPbI_3$ has a lower stiffness and is vulnerable to deform, which is of benefit to get a high-quality wafer.[33] Moreover, benefiting from the lower Young's modulus of supple δ-$FAPbI_3$, we have demonstrated that the lower residual stresses in δ-$FAPbI_3$ wafers through d-$\sin^2(\Psi)$ method and finite element simulations. The low residual stress can help δ-$FAPbI_3$ wafer form a more compact structure and facilitate the long-term structural stability of the device (details see Fig. S12-14). Correspondingly, the mercury intrusion porosimetry (MIP) method was performed,[34] Fig. 2e showed that the pore size distribution in the δ-$FAPbI_3$ wafer is significantly smaller than that of the α-$FAPbI_3$ wafer. And the porosity of α-$FAPbI_3$ wafer (7.51 %) is more than twice that of δ-$FAPbI_3$ wafer (3.49 %), indicating superior compactness of δ-$FAPbI_3$ wafer.

The detailed micromorphology of the wafers was further investigated by SEM (Fig. 2f and Fig. S15). The δ-$FAPbI_3$ wafer exhibits a homogeneous and dense surface with less grain boundaries. The corresponding cross-sectional SEM (Fig. 2g) also shows that the large agglomerated blocks of δ-$FAPbI_3$ are tightly bound together, exhibiting a

compact and nonporous morphology. In contrast, the α-$FAPbI_3$ wafer has a rougher surface and smaller crystals with numerous holes between the grain boundaries (Fig. 2h, i).

Based on the above analysis, we propose schematic models of the two wafers (Fig. 2b): the δ-$FAPbI_3$ wafer with flat and compact structure ensured stable photo carrier transport and effective charge extraction, while the numerous voids and internal defects in α-$FAPbI_3$ wafer not only hamper the device collection efficiency, but also lead to severe ion migration, significant baseline drifting, and signal acquisition jamming. The better morphology of the δ-$FAPbI_3$ comes from the precursor. As the single crystal pre-assembly in the solution forms rod-shaped blocks, the δ-$FAPbI_3$ powder with wide particle size distribution tends to have better packing density (Fig. S16).[35] And the plastic deformation of the supple δ-$FAPbI_3$ powder during the pressing process is more conducive to forming compact wafers with less porosity and low residual stress . Additionally, high quality δ-$FAPbI_3$ wafers can be fabricated using a simple compressing process, avoiding the high temperature treatment widely used in other works,[13, 15, 36] implying a great competitiveness in commercial applications.

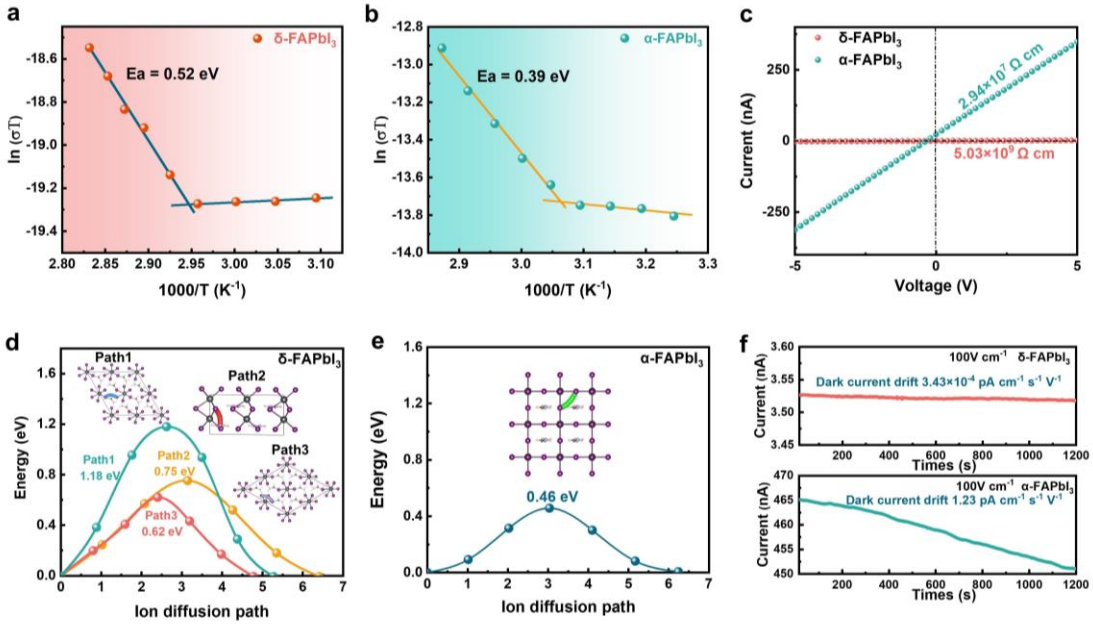

Figure 3. Ionic migration in δ-$FAPbI_3$ and α-$FAPbI_3$. Temperature-dependent conductivity of the (a) δ-$FAPbI_3$ wafer and (b) α-$FAPbI_3$ wafer. (c) The resistivity of δ-$FAPbI_3$ and α-$FAPbI_3$ wafers.

Calculated energy profiles along the different I^- ion-migration paths in (d) 1D δ-$FAPbI_3$ and (e) 3D α-$FAPbI_3$. (f) Dark current drift of the δ-$FAPbI_3$ and α-$FAPbI_3$ detectors at an electric field of 100 V cm^{-1}.

Ionic migration in the wafers

Previous reports have noted that ion migration inside wafer devices can lead to severe baseline drift and damage the crystal structure of the halide perovskite crystal, and correspondingly decrease the sensitivity of the detector and reduce the lifetime of the device.[15, 16] To assess the ion mobility levels, we measured the conductivity of the wafers at different temperatures, and the activation energy (E_a) of ionic migration can be obtained by fitting the Nernst-Einstein relationship curve.[14]

$$\sigma(T) = (\frac{\sigma_0}{T})\ exp(-\frac{E_a}{k_B T}) \qquad (1)$$

Where T is the temperature, $\sigma(T)$ is the conductivity, σ_0 is a constant, k_B is the Boltzmann constant and E_a is activation energy of ion conduction. As shown in Fig. 3 (a, b), with increasing temperature, the conductivity of δ-$FAPbI_3$ wafer remains almost constant at the low temperature stage, which refers to electronic conduction region. Then, the total conductivity of the δ-$FAPbI_3$ wafer shows a rapid increase when the temperature reached 340 K, corresponding to the ionic conduction being thermally activated and dominating the conductivity.[37] By measuring the slope of the conductivity dependence, the E_a of δ-$FAPbI_3$ wafer can be calculated as 0.52 eV, which is higher than that of α-$FAPbI_3$ (0.39 eV) and even $MAPbI_3$ (0.19 eV), indicating significantly lower ion migration in δ-$FAPbI_3$ wafer. Correspondingly, the resistivity of the δ-$FAPbI_3$ wafer is 5.03×10^9 Ω cm, which is higher than that of the α-$FAPbI_3$ (2.94×10^7 Ω cm) (Fig. 3c), leading to lower dark current and further decreased detection limit.

We further investigated the differences of I^- ion-migration behavior in the 1D δ-$FAPbI_3$ and 3D α-$FAPbI_3$ via density functional theory (DFT). Several reports have shown that the ion migration in halide perovskite is dominated by I^- migration, resulting from the weak Pb-I bond and the short ion migration distance, whereas significant Pb^{2+} and FA^+ migrations are less probable owing to their high activation energy.[16, 38] Hence, we simulated three different paths of iodide ion migration to the nearby iodine vacancy in

1D δ-$FAPbI_3$ crystal cells using the climbing image nudged elastic band (CINEB) method. Each migration route was divided into seven steps (initial state, five inter-transition states and the final state), and the energy barrier is calculated from the difference between the total energies of initial state and the saddle point. Fig. 3d illustrates the energy barriers for the three possible migration paths in δ-$FAPbI_3$ are 1.18, 0.75 and 0.62 eV. One migration path in 3D α-$FAPbI_3$ was be considerate because the diffusion routes are isotropic (Fig. 3e), and the iodide ion energy barriers (0.46 eV) in α-$FAPbI_3$ is lower than that of 1D δ-$FAPbI_3$, indicating that the migration of I^- in 1D δ-$FAPbI_3$ is considerably inhibited. This can be explained by the fact that the face-sharing octahedra in δ-$FAPbI_3$ only propagating along the (001) orientation and disconnected to the other directions, thus leading to the ion migration channels being reduced compared to the three-dimensional structure.

Generally, high activation energy of ionic migration and high resistance can substantially enhance the stability of the δ-$FAPbI_3$ detector under a high electric field. As shown in Fig.3f, the long-term dark current of δ-$FAPbI_3$ and α-$FAPbI_3$ wafers exhibited significant differences. 1D δ-$FAPbI_3$ detector maintain a stable current baseline at ~3.53 nA for 1200 s under 100V cm^{-1} electric field, while the α-$FAPbI_3$ detector shows a noticeable baseline drift at ~ 460 nA. The following formulation was adopted to calculate the dark current drift:

$$I_{drift} = (I_t - I_0)/E \times S \times t \qquad (2)$$

Where I_t and I_0 is the current at the ending and beginning state, E is the electric field and S is the detector area.[39] The calculated current drift of δ-$FAPbI_3$ detector was 3.43 × 10^{-4} pA cm^{-1} s^{-1} V^{-1}, and this ultra-stable baseline is almost comparable to that of a single crystal perovskite detector.[39] In contrast, α-$FAPbI_3$ detector exhibits 1.23 pA cm^{-1} s^{-1} V^{-1} current drift, equivalent to previously reported $MAPbI_3$ (0.13 pA cm^{-1} s^{-1} V^{-1}), both of which are several orders of magnitude larger than that of δ-$FAPbI_3$ detector. This difference could be attributed to the low ion migration and highly compact structure of 1D δ-$FAPbI_3$ wafer.

Subsequently, the time-of-flight (TOF) method was employed to determine the carrier mobility (μ) of δ-$FAPbI_3$ wafers (see experimental section for details). With the excitation of a pulsed laser, the charge drift time (t_{tr}) can be obtained by analyzing the pulse height rise time distribution, and the mobility can be calculated from the formulation: $\mu = d^2 / (V t_{tr})$, where d is the wafer thickness and V is the bias.[40] The typical TOF results are shown in Fig. S17 and S18, the hole and electron mobility of the δ-$FAPbI_3$ wafer are 2.07-5.92 $cm^2 V^{-1} s^{-1}$ and 2.41-6.54 $cm^2 V^{-1} s^{-1}$, respectively. And the comparable value of μ for electrons and holes indicates an ambipolar charge transport in δ-$FAPbI_3$ wafers (Fig. S19).

For practical applications, the stability of the semiconductor in air atmosphere is also a key property. The thermodynamic stability of α-$FAPbI_3$ and δ-$FAPbI_3$ were examined by DFT calculating (Table S2). The binding energies were calculated to be -0.414 eV and -0.422 eV per atom for α-$FAPbI_3$ and δ-$FAPbI_3$, respectively. Suggesting that δ-$FAPbI_3$ has a more stable thermodynamically stable structure. Correspondingly, as shown in Fig. S20, the δ-$FAPbI_3$ wafer shows no significant changes in the XRD patterns after exposure for 6 months in ambient air with a relative humidity of ≈70±5%, demonstrating superior environmental stability.[41]

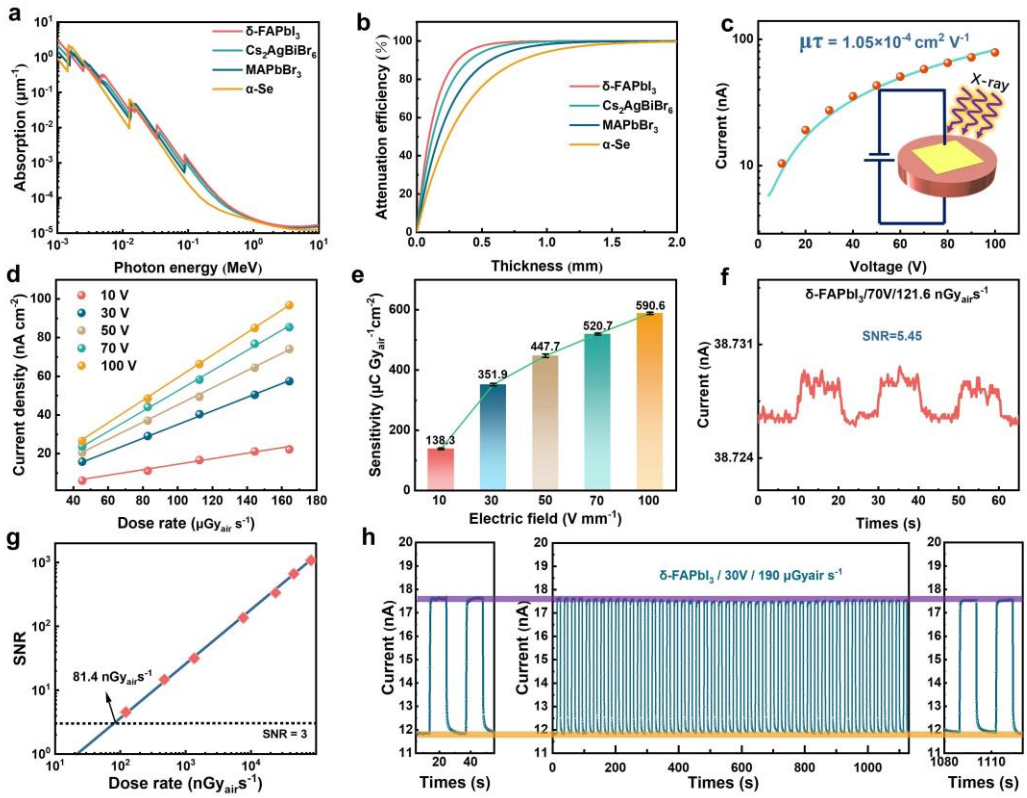

Figure 4. X-Ray detection performance of the δ-$FAPbI_3$ wafer detectors. (a) Absorption coefficients of δ-$FAPbI_3$ $Cs_2AgBiBr_6$, $MAPbBr_3$ and a-Se as a function of photon energy; (b) Attenuation efficiency of δ-$FAPbI_3$ $Cs_2AgBiBr_6$, $MAPbBr_3$ and a-Se for 40 keV X-ray photons versus thickness; (c) Bias-dependent photoconductivity of the Au/δ-$FAPbI_3$ /Au device and the derived μτ value under X-ray; (d) Signal current densities as a function of dose rate at different applied electric fields under X-ray; (e) Sensitivity under different electric field of the δ-$FAPbI_3$ wafer X-ray detector; (f) X-ray response characteristics of the δ-$FAPbI_3$ detector under an ultralow X-ray dose rates (121.6 nGy_{air} s^{-1}) at 70 Vmm^{-1} electric field; (g) Dose rate dependent SNR of the δ-$FAPbI_3$ detector; (h) Stability of the X-ray response of the δ-$FAPbI_3$ detector.

Performance of X-ray detectors

High resistivity, low ion migration, stable current baseline and long-term stability are essential for high-performance photodetectors, as aforementioned analysis, 1D δ-$FAPbI_3$ wafer was qualified and a promising candidate for commercial X-ray detector.

With the aim of fabricate high quality X-ray detectors, it is essential to select the optimum thickness to ensure sufficient absorption of X-rays, yet minimize the transmission distance of photocarriers. Here, the continuum bremsstrahlung X-ray equipment operated at a voltage of 50 kV, and the mean energy was calibrated as 33.93 keV (Fig. S21). The absorption coefficients of perovskites and traditional semiconductors are obtained from the NIST database, the absorption coefficient of $FAPbI_3$ is close to that of the double perovskite $Cs_2AgBiBr_6$ while higher than that of $MAPbBr_3$ and a-Se (Fig. 4a).[42] The high absorption coefficient corresponds to the high attenuation coefficient, which supports that 0.8 mm thickness of $FAPbI_3$ can attenuate 99.7 % of the 40 keV X-ray photons (Fig. 4b). For guarantying sufficient X-ray absorption, the 0.8 mm thickness wafer is selected and assembled it into vertical structure (Au/ $FAPbI_3$ /Au) for further testing.

Mobility-lifetime products ($\mu\tau$) is a key parameter to estimate a semiconductor's capability of extracting charge, we thus recorded the photoconductivity of δ-$FAPbI_3$ wafer under a 50 kV_p X-ray excitation source, and obtained the $\mu\tau$ product by fitting with the Hecht equation. As exhibited in (Fig. 4c), δ-$FAPbI_3$ wafer held a $\mu\tau$ product of 1.05×10^{-4} cm^2 V^{-1}, which is close to 3D $MAPbI_3$ wafers (2×10^{-4} cm^2 V^{-1}) and slightly lower than $Cs_3Bi_2I_9$ single crystal detector (7.97×10^{-4} cm^2 V^{-1}), while superior to the a-Se (10^{-7} cm^2 V^{-1}).[13, 42, 43]

Besides, the on/off photocurrent response under various electric fields (from 10 to 100V) and dose rates (45.1-192.4 μGy_{air} s^{-1}) are listed in Fig. S22-24, respectively. It can be concluded that the δ-$FAPbI_3$ detector has steady current signal and good reproducibility. Meanwhile, the generated photocurrent density scaled linearly with the X-ray dose rate (Fig. 4d). And the sensitivity of the δ-$FAPbI_3$ wafer detector under different biases can be calculated by fitting the slope of the photocurrent density-dose rate curves. As shown in Fig. 4e, with the increase of electric field from 10 to 100 V mm^{-1}, the sensitivity of the detector shows an increasing trend, owing to the higher electric field contributing to better charge collection. Under 100 V mm^{-1} field, the δ-$FAPbI_3$ wafer detector can reach a sensitivity of 590.6 μC Gy_{air}^{-1} cm^{-2}, which is almost

thirty times higher than that for the a-Se X-ray detectors (20 μC Gy_{air}^{-1} cm^{-2} at a higher field of 10 V μm^{-1}).[44]

In addition to the sensitivity, the LoD is also a crucial parameter for evaluating the detectors performance, Fig. 4f shows the response of the δ-$FAPbI_3$ wafer detector under X-ray dose rates of 121.6 nGy_{air} s^{-1} at 70 Vmm^{-1} electric field, and the signal to noise ratios (SNR) of detector is calculate as 5.45, indicating its high detection efficiency at low radiation doses. Effective detection required the generated signal three times higher than the noise level.[45] By fitting the SNR at various radiation doses (Fig. 4g), we obtained the LoD of 81.4 nGy_{air} s^{-1}, which is much lower than the requirement of conventional medical diagnostics (5.5 μGy_{air} s^{-1}). The comparison of the δ-$FAPbI_3$ detector with other perovskite-based wafer devices reported previously was list in Table S3. What's more, Fig. 4h shows the response of δ-$FAPbI_3$ wafer detector under on/off X-ray radiation for long term testing. The δ-$FAPbI_3$ detector presents steady current signal with no photocurrent signal attenuation or baseline current drift, and there is almost no degradation in response current for δ-$FAPbI_3$ wafer aging for 6 months (Fig. S25), demonstrating its great operational and irradiation stability.

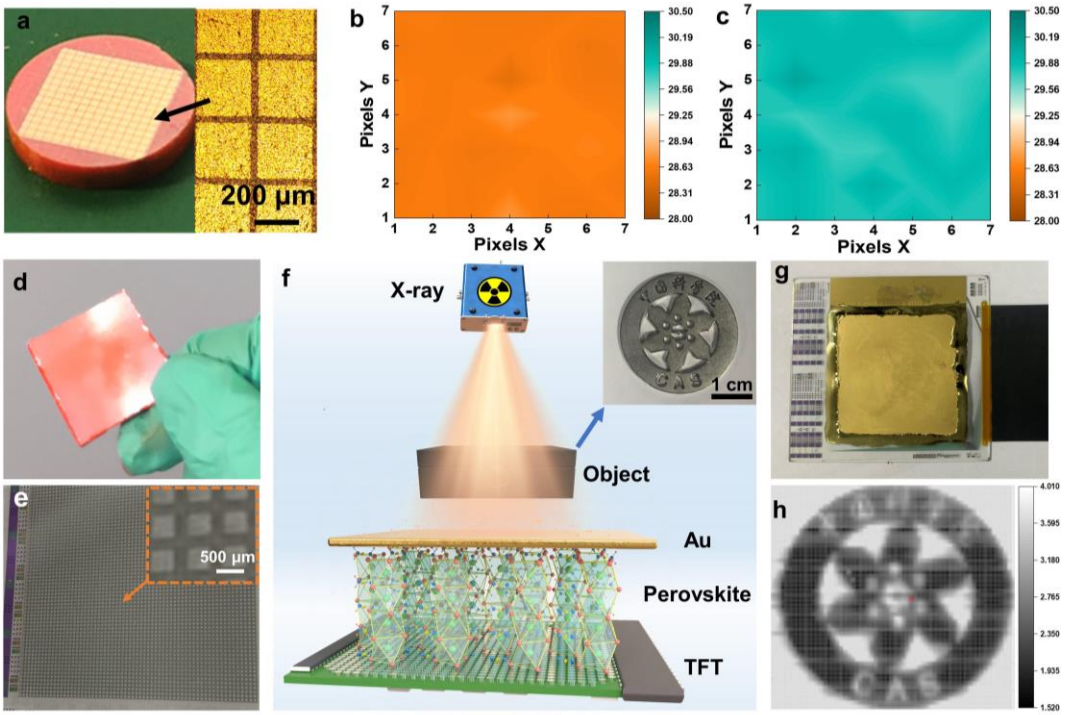

Figure 5. X-Ray imaging performance of the δ-$FAPbI_3$ wafer detectors: (a) The prepared 14×14 pixels wafer-based detector; (b) Mapping of dark current and (c) photocurrent; (d) Fabrication of 3×3 cm δ-$FAPbI_3$ wafer by cold isostatic-pressing; (e) Microstructure of the 64×64 pixels TFT backplane, the pixel pitch is 500 μm; (f) Schematic illustration of the X-ray imaging process using a δ-$FAPbI_3$ wafer X-ray imaging detector, the inset is the optical image of tested object; (g) Photograph of the final flat-panel X-ray imaging detector. (h) X-ray imaging of the "Chinese Academy of Sciences" logo.

X-ray imaging performance

The uniformity of the detector determines the clear distinction of gray levels, which is directly related to the quality of imaging.[15] In order to test the uniformity of the δ-$FAPbI_3$ wafer device, we prepared a 14×14 pixels detector using the laser cutting method **(**Fig. 5a), in which a 7×7 pixels array was selected for testing responses under dark and light conditions. Fig. 5b and c showed the value of dark current as 28.51±0.05 nA and of photocurrent as 29.89±0.08 nA, respectively. The standard deviation of dark and light signals is both much lower than the value of signal current, proving a good uniformity of the wafer device. Then the modulation transfer function (MTF) of the δ-$FAPbI_3$ wafer was measured, as shown in Fig. S26, the resolution of δ-$FAPbI_3$ wafer is 4.0 at MTF=20%, demonstrating its excellent imaging capability and is capable for millimeter scale imaging.

We further assembled pixels array detector to realize direct flat panel radiographic imaging. A 3×3 cm size of δ-$FAPbI_3$ wafer with 0.8 mm thickness was fabricated by cold isostatic-pressing (Fig. 5d) with good flatness and gloss, implying the upgradeability of this method. Subsequently, the wafer was integrated as a photoconductor with a 64×64 pixels thin film transistor (TFT) backplane (Fig. 5e), using an electronic bonding agent around the wafer for fixing. The prepared flat-panel direct detectors (Fig. 5g) were further applied to radiography imaging. As illustrated in Fig. 5f, the X-rays emitted by the ray tube will be absorbed when they pass through the metal sample object, and the pixel electrodes at different positions will receive a different photo response current. The electrical signals are collected by the matrix

electrodes and exported to external devices through the readout circuit. Ultimately, the shape characteristics of the object can be obtained by analyzing the electrical signal intensity distribution. As a result, the radiograph offers a detailed view of the metal sample with a sufficient resolution to clearly recognize the characters (Fig. 5h).

Conclusion

In summary, we developed a high-performance X-ray wafer detector, and found the hexagonal δ-$FAPbI_3$ perovskite derivative has significantly low ionic migration, low Young's modulus and excellent long-term stability, which allow us to prepare a highly compact and low residual stress wafer for high-performance X-ray detector. As a result, the detector showed an ultralow dark current drift of 3.43×10^{-4} pA cm^{-1} S^{-1} V^{-1}, combined with a low detection limit of 81.4 nGy_{air} s^{-1} and long-term stability. The device achieved high sensitivity of 590.6 μC Gy_{air}^{-1} cm^{-2} under 50 kV_p X-ray, which is about thirty times higher than that of commercial a-Se X-ray detectors. Notably, the δ-$FAPbI_3$ wafer detector enables direct multi-pixel X-ray imaging by integrating a large size δ-$FAPbI_3$ wafer with TFT backplane. The high stability, good detection performance, and outstanding X-ray imaging property of 1D δ-$FAPbI_3$ render it a highly promising candidate for X-ray detection. Our findings also suggest the preparation of multi-pixel wafer X-ray imaging detector has immense potential for commercial X-ray detector application.

Methods

Synthesis of FAI

Formamidinium iodide (FAI) was synthesized by reacting formamidine acetate (0.1 mol, 98%) with hydriodic acid (0.1 mol, 57 wt% in water, sigma-aldrich) in a flask and were stirred at 0 °C for 2 h. The yellow powder was obtained by evaporation of the solvent

at 60 °C for 1 h. Then the product was recrystallized three times by dissolving in ethanol, and cleaned by diethyl ether. The resulting product was dried in a vacuum oven for 24h.

Fabricate of α-$FAPbI_3$ powders

The α-$FAPbI_3$ powders were synthesized by a solvent evaporation method. PbI_2 (1.537 g) and FAI (0.47 g) were dissolved in 15ml γ-butyrolactone (GBL), and the precursor solution was put into a glass beaker and kept stirring for 3 h. The beaker was then placed on a heating table at 150 °C, the black α-$FAPbI_3$ powder was obtained with the dissolved evaporation totally. The resulting product cleaned by diethyl ether 6 times and completely dried at 40 °C in a vacuum oven for 12h.

δ-$FAPbI_3$ wafers Fabrications

The massive bulky single-crystal aggregates were synthesized by wet chemistry reaction based on antisolvents.1.537 g PbI (99.99%, Alfa Aesar) and 0.47 g FAI were mixed by grinding, then the mixture was added in to 20 ml sample bottles containing 15 mL acetonitrile (ACN) and stirred at high speed for 30 h. The resulting product was cleaned with diethyl ether for 6 times and completely dried at 40 °C in a vacuum oven for 12 h. The δ-$FAPbI_3$ powders were then placed into the 5×5 mm mold, which was pressed at 200 MPa for 20 min, and high quality δ-$FAPbI_3$ wafers with high density and low porosity can be obtained. The larger sized 3×3 cm δ-$FAPbI_3$ wafer was fabricated in the same way. The same cold isostatic compression conditions were used to prepare 5×5 mm α-$FAPbI_3$ wafers as control samples

Device fabrication

Au/δ-$FAPbI_3$ wafers/Au devices were employed for X-ray detection measurements. The Au electrodes (80 nm) with a size of 3×3 mm was deposited vertically on the top and bottom of the perovskite wafer by thermal evaporation, the thickness of the wafer was 0.8 mm for sufficient absorption of the 50 keV X-ray. For the TOF measurements, the 3×3 mm Au charge-collecting electrodes with thicknesses of 40 and 80 nm were

thermally evaporated on both sides of the δ-$FAPbI_3$ wafers (1 mm), respectively, and the thin side was used as the semitransparent electrode for light transmission.

Materials Characterization

X-ray diffraction (XRD) patterns of the perovskite were performed with a Rigaku Smartlab 9 kW diffractometer with Cu Ka radiation. Morphologies of the perovskite powder and wafer were characterized by scanning electron microscopy (SEM, Hitachi SU8020) with a Schottky Field Emission gun, High resolution transmission electron microscope TEM (HRTEM) operated at 200 kV was used for further Structural morphology analysis. Mercury intrusion porosimetry (MIP) was used to measure porosities of the perovskite wafers. Absorption spectra and Steady-state photo luminescence (PL) spectra were measured using ultraviolet (UV) spectrophotometer (U-3900H) and spectrofluorometer (Photon Technology International), respectively. High precision micrometer was used to measure the thickness of the wafers. The Nanoindentation was performed on a in-situ nanomechanical test system (TI-950, HYSITRON).

Hole and electron mobilities measured

Hole and electron mobilities were measured by the time-of-flight (TOF) method, A pulsed laser with 532 nm wavelength and 6 ns width was illuminated on the 40 nm semitransparent Au electrode of the device. A Keithley digital source meter (Model 2400) was used to apply a bias to the sample and the photocurrent was recorded with a low-noise current preamplifier (SR570, Stanford Research Systems). When the 40 nm semitransparent Au electrode is used as the cathode, the hole mobility can be calculated based on the transition time of the photogenerated holes between the opposite electrodes. Similarly, when this electrode is used as the anode, the electrons mobility can be calculated based on the transition time of the photogenerated electrons between the opposite electrodes.

X-ray detection Measurement and imaging

We chose a tungsten anode X-ray tube with ~ 2.5 mm Al filter as the source to investigate the X-ray detection performance. The X-ray source worked under a constant 50 kV voltage and modulated the radiation dose rate by changing the tube current (0.2-0.5 mA). Further, X-ray dose rate was calibrated using a Radcal Accu-Dose^{+} 10×6-180 dosimeter. The I-t characteristics were measured with a Keithley 6517b source meter operated by Wu Han ZY Technology software. All tests were performed in an anti-radiation lead box, in order to decrease electromagnetic signal effects and interference from ambient light. For X-ray imaging, a 3×3 cm size δ-$FAPbI_3$ wafer was integrated onto the TFT substrate backplane (the TFT backplane and readout circuit system were provided by LinkZill), followed by fixing the wafer with electronic adhesive and curing under 5 mPa for 24 hours. Finally, the top surface of the device was covered with 100 nm gold as the top electrode. The flat-panel detector was worked under 192.4 $\mu Gy_{air}\ s^{-1}$ dose rate with 10V bias for imaging, The sample size of pixel value distribution in detector was 4096, each pixel has a grayscale value between 0 and 255.

Computational details

First-principle calculations in this work were performed in the framework of the density functional theory (DFT) with the projector augmented plane-wave method, as implemented in the Vienna ab initio simulation package (VASP). The generalized gradient approximation proposed by Perdew–Burke–Ernzerhof (PBE), is selected for the exchange-correlation potential. The cut-off energy for a plane wave is set to 500 eV. The energy criterion is set to 10^{-5} eV in the iterative solution of the Kohn-Sham equation. The Brillouin zone integration is performed using a 5×5×5 k-mesh. All the structures are relaxed until the residual forces on the atoms have declined to less than 0.02 eV/Å. The energy barriers for I ion diffusion in the perovskite were computed by the nudged elastic band (CI-NEB) method with 5 images. The Finite Element Model (FEM) analysis was conducted using COMSOL Multiphysics, and the residual stress distribution within wafers was assessed based on Density-dependent Drucker–Prager Cap (DPC) model.

Acknowledgements

The authors acknowledge financial support from National Key R&D Program of China (No.2021YFB3800102) The Science Funds of Distinguished Young Scholars of Anhui Province (Grant No. 2108085J34). Key Lab of Photovoltaic and Energy Conservation Materials, Chinese Academy of Sciences (Grant No. PECL2021QN002) and CASHIPS Director's Fund (YZJJ202304-CX). X. Zheng acknowledges the financial support from National Natural Science Foundation of China (Grant No. NSFC62004182) and the Sichuan Science and Technology Program (Grant No. 2022JDRC0021).

Author contributions

J.Y. and X.P. conceived the idea and supervised the project. Z.W. designed the experiments. Z.W. and S.T. carried out material preparation, characterizations and device fabrication. Z.W., H.Z. and C.W. set up the measurement facilities for the X-ray detector and photodetector. Z.W., S.T. and H.Z. measured the detector optoelectronic characterizations, X-ray detector response and imaging. Z.L. and H.X. assisted with the measurement and discussions. J.Y. and Z.W. co-wrote the manuscript, and X.Z., A.D. and R.P. provided the revisions. All the authors reviewed the paper.

Competing interests

The authors declare no competing interests

Additional information

Reference

(1) Wei, H.; Huang, J., Halide Lead Perovskites for Ionizing Radiation Detection. *Nat. Commun.* **2019,** *10* (1), 1066.

(2) Yakunin, S.; Sytnyk, M.; Kriegner, D.; Shrestha, S.; Richter, M.; Matt, G. J.; Azimi, H.; Brabec, C. J.; Stangl, J.; Kovalenko, M. V.; Heiss, W., Detection of X-Ray Photons by Solution-Processed Lead Halide Perovskites. *Nat. Photonics* **2015,** *9* (7), 444-449.

(3) Wei, H. T.; Fang, Y. J.; Mulligan, P.; Chuirazzi, W.; Fang, H. H.; Wang, C. C.; Ecker, B. R.; Gao, Y. L.; Loi, M. A.; Cao, L.; Huang, J. S., Sensitive X-Ray Detectors Made of Methylammonium Lead Tribromide Perovskite Single Crystals. *Nat. Photonics* **2016,** *10* (5), 333-339.

(4) Nikl, M.; Yoshikawa, A., Recent R&D Trends in Inorganic Single-Crystal Scintillator Materials for Radiation Detection. *Adv. Opt. Mater.* **2015,** *3* (4), 463-481.

(5) Kakavelakis, G.; Gedda, M.; Panagiotopoulos, A.; Kymakis, E.; Anthopoulos, T. D.; Petridis, K., Metal Halide Perovskites for High-Energy Radiation Detection. *Adv. Sci.* **2020,** *7* (22), 2002098.

(6) Eisen, Y.; Shor, A.; Mardor, I., Cdte and Cdznte X-Ray and Gamma-Ray Detectors for Imaging Systems. *IEEE Nuclear Science Symposium/Medical Imaging Conference* **2003**, 3311-3319.

(7) Xu, X.; Qian, W.; Xiao, S.; Wang, J.; Zheng, S.; Yang, S., Halide Perovskites: a Dark Horse for Direct X‐Ray Imaging. *EcoMat* **2020,** *2* (4), 12064.

(8) Qian, W.; Xu, X.; Wang, J.; Xu, Y.; Chen, J.; Ge, Y.; Chen, J.; Xiao, S.; Yang, S., An Aerosol-Liquid-Solid Process for the General Synthesis of Halide Perovskite Thick Films for Direct-Conversion X-Ray Detectors. *Matter* **2021,** *4* (3), 942-954.

(9) Glushkova, A.; Andricevic, P.; Smajda, R.; Nafradi, B.; Kollar, M.; Djokic, V.; Arakcheeva, A.; Forro, L.; Pugin, R.; Horvath, E., Ultrasensitive 3D Aerosol-Jet-

Printed Perovskite X-Ray Photodetector. *ACS Nano* **2021,** *15* (3), 4077-4084.

(10) Li, Z.; Zhou, F.; Yao, H.; Ci, Z.; Yang, Z.; Jin, Z., Halide Perovskites for High-Performance X-Ray Detector. *Mater. Today* **2021,** *48*, 155-175.

(11) Kundu, S.; Richtsmeier, D.; Hart, A.; Yeddu, V.; Song, Z.; Niu, G.; Thrithamarassery Gangadharan, D.; Dennis, E.; Tang, J.; Voznyy, O.; Bazalova-Carter, M.; Saidaminov, M. I., Orthorhombic Non-Perovskite $CsPbI_3$ Microwires for Stable High-Resolution X-Ray Detectors. *Adv. Opt. Mater.* **2022,** *10* (13), 2200516.

(12) Li, M. B.; Li, H. Y.; Li, W. J.; Li, B.; Lu, T.; Feng, X. P.; Guo, C. J.; Zhang, H. M.; Wei, H. T.; Yang, B., Oriented 2D Perovskite Wafers for Anisotropic X-ray Detection through a Fast Tableting Strategy. *Adv. Mater.* **2022,** *34* (8), 2108020.

(13) Shrestha, S.; Fischer, R.; Matt, G. J.; Feldner, P.; Michel, T.; Osvet, A.; Levchuk, I.; Merle, B.; Golkar, S.; Chen, H.; Tedde, S. F.; Schmidt, O.; Hock, R.; Rührig, M.; Göken, M.; Heiss, W.; Anton, G.; Brabec, C. J., High-Performance Direct Conversion X-Ray Detectors Based on Sintered Hybrid Lead Triiodide Perovskite Wafers. *Nat. Photonics* **2017,** *11* (7), 436-440.

(14) Tie, S.; Zhao, W.; Xin, D.; Zhang, M.; Long, J.; Chen, Q.; Zheng, X.; Zhu, J.; Zhang, W. H., Robust Fabrication of Hybrid Lead-Free Perovskite Pellets for Stable X-ray Detectors with Low Detection Limit. *Adv. Mater.* **2020,** *32* (31), 2001981.

(15) Yang, B.; Pan, W. C.; Wu, H. D.; Niu, G. D.; Yuan, J. H.; Xue, K. H.; Yin, L. X.; Du, X. Y.; Miao, X. S.; Yang, X. Q.; Xie, Q. G.; Tang, J., Heteroepitaxial Passivation of $Cs_2AgBiBr_6$ Wafers with Suppressed Ionic Migration for X-Ray Imaging. *Nat. Commun.* **2019,** *10*, 1989.

(16) Eames, C.; Frost, J. M.; Barnes, P. R. F.; O'Regan, B. C.; Walsh, A.; Islam, M. S., Ionic Transport in Hybrid Lead Iodide Perovskite Solar Cells. *Nat. Commun.* **2015,** *6*, 7497.

(17) Xiao, Z. G.; Yuan, Y. B.; Shao, Y. C.; Wang, Q.; Dong, Q. F.; Bi, C.; Sharma, P.; Gruverman, A.; Huang, J. S., Giant Switchable Photovoltaic Effect in Organometal Trihalide Perovskite Devices. *Nat. Mater.* **2015,** *14* (2), 193-198.

(18) Kim, Y. C.; Kim, K. H.; Son, D. Y.; Jeong, D. N.; Seo, J. Y.; Choi, Y. S.; Han, I. T.;

Lee, S. Y.; Park, N. G., Printable Organometallic Perovskite Enables Large-Area, low-Dose X-Ray Imaging. *Nature* **2017,** *550* (7674), 87-91.

(19) McMeekin, D. P.; Sadoughi, G.; Rehman, W.; Eperon, G. E.; Saliba, M.; Horantner, M. T.; Haghighirad, A.; Sakai, N.; Korte, L.; Rech, B.; Johnston, M. B.; Herz, L. M.; Snaith, H. J., A Mixed-Cation Lead Mixed-Halide Perovskite Absorber for Tandem Solar Cells. *Science* **2016,** *351* (6269), 151-155.

(20) Hoke, E. T.; Slotcavage, D. J.; Dohner, E. R.; Bowring, A. R.; Karunadasa, H. I.; McGehee, M. D., Reversible Photo-Induced Trap Formation in Mixed-Halide Hybrid Perovskites for Photovoltaics. *Chem. Sci.* **2015,** *6* (1), 613-617.

(21) Conings, B.; Drijkoningen, J.; Gauquelin, N.; Babayigit, A.; D'Haen, J.; D'Olieslaeger, L.; Ethirajan, A.; Verbeeck, J.; Manca, J.; Mosconi, E.; De Angelis, F.; Boyen, H. G., Intrinsic Thermal Instability of Methylammonium Lead Trihalide Perovskite. *Adv. Energy Mater.* **2015,** *5* (15), 1500477.

(22) Ma, F.; Li, J.; Li, W.; Lin, N.; Wang, L.; Qiao, J., Stable Alpha/Delta Phase Junction of Formamidinium Lead Iodide Perovskites for Enhanced Near-Infrared Emission. *Chem. Sci.* **2017,** *8* (1), 800-805.

(23) Zhang, Y.; Seo, S.; Lim, S. Y.; Kim, Y.; Kim, S.-G.; Lee, D.-K.; Lee, S.-H.; Shin, H.; Cheong, H.; Park, N.-G., Achieving Reproducible and High-Efficiency (>21%) Perovskite Solar Cells with a Presynthesized $FAPbI_3$ Powder. *ACS Energy Lett.* **2019,** *5* (2), 360-366.

(24) Han, Q.; Bae, S. H.; Sun, P.; Hsieh, Y. T.; Yang, Y. M.; Rim, Y. S.; Zhao, H.; Chen, Q.; Shi, W.; Li, G.; Yang, Y., Single Crystal Formamidinium Lead Iodide ($FAPbI_3$): Insight into the Structural, Optical, and Electrical Properties. *Adv. Mater.* **2016,** *28* (11), 2253-8.

(25) Stoumpos, C. C.; Malliakas, C. D.; Kanatzidis, M. G., Semiconducting Tin and Lead Iodide Perovskites with Organic Cations: Phase Transitions, High Mobilities, and Near-Infrared Photoluminescent Properties. *Inorg. Chem.* **2013,** *52* (15), 9019-38.

(26) Zhang, Y.; Ma, Y.; Wang, Y.; Zhang, X.; Zuo, C.; Shen, L.; Ding, L., Lead-Free Perovskite Photodetectors: Progress, Challenges, and Opportunities. *Adv. Mater.* **2021,**

33 (26), 2006691.

(27) Jana, M. K.; Song, R.; Liu, H.; Khanal, D. R.; Janke, S. M.; Zhao, R.; Liu, C.; Valy Vardeny, Z.; Blum, V.; Mitzi, D. B., Organic-to-Inorganic Structural Chirality Transfer in a 2D Hybrid Perovskite and Impact on Rashba-Dresselhaus Spin-Orbit Coupling. *Nat. Commun.* **2020,** *11* (1), 4699.

(28) Weller, M. T.; Weber, O. J.; Frost, J. M.; Walsh, A., Cubic Perovskite Structure of Black Formamidinium Lead Iodide, α-$[HC(NH_2)_2]PbI_3$, at 298 K. *J. Phys. Chem. Lett.* **2015,** *6* (16), 3209-3212.

(29) Jiang, S.; Luan, Y.; Jang, J. I.; Baikie, T.; Huang, X.; Li, R.; Saouma, F. O.; Wang, Z.; White, T. J.; Fang, J., Phase Transitions of Formamidinium Lead Iodide Perovskite under Pressure. *J. Am. Chem. Soc.* **2018,** *140* (42), 13952-13957.

(30) Sun, S.; Isikgor, F. H.; Deng, Z.; Wei, F.; Kieslich, G.; Bristowe, P. D.; Ouyang, J.; Cheetham, A. K., Factors Influencing the Mechanical Properties of Formamidinium Lead Halides and Related Hybrid Perovskites. *ChemSusChem* **2017,** *10* (19), 3740-3745.

(31) Li, Z.; Qin, Y.; Dong, L.; Li, K.; Qiao, Y.; Li, W., Elastic and Electronic Origins of Strain Stabilized Photovoltaic Gamma-$CsPbI_3$. *Phys. Chem. Chem. Phys.* **2020,** *22* (22), 12706-12712.

(32) Li, S.; Zhao, S.; Chu, H.; Gao, Y.; Lv, P.; Wang, V.; Tang, G.; Hong, J., Unraveling the Factors Affecting the Mechanical Properties of Halide Perovskites from First-Principles Calculations. *The Journal of Physical Chemistry C* **2022,** *126* (9), 4715-4725.

(33) Sun, W.-J.; Kothari, S.; Sun, C. C., The Relationship Among Tensile Strength, Young's Modulus, and Indentation Hardness of Pharmaceutical Compacts. *Powder Technol.* **2018,** *331*, 1-6.

(34) Zeng, Q.; Li, K.; Fen-chong, T.; Dangla, P., Pore Structure Characterization of Cement Pastes Blended with High-Volume Fly-Ash. *Cem. Concr. Res.* **2012,** *42* (1), 194-204.

(35) Mostafaei, A.; Rodriguez De Vecchis, P.; Nettleship, I.; Chmielus, M., Effect of Powder Size Distribution on Densification and Microstructural Evolution of Binder-Jet

3D-Printed Alloy 625. *Mater. Des.* **2019,** *162*, 375-383.

(36) Liu, W.; Shi, T.; Zhu, J.; Zhang, Z.; Li, D.; He, X.; Fan, X.; Meng, L.; Wang, J.; He, R.; Ge, Y.; Liu, Y.; Chu, P. K.; Yu, X. F., PbI_2-DMSO Assisted In Situ Growth of Perovskite Wafers for Sensitive Direct X-Ray Detection. *Adv. Sci.* **2022,** *10* (1), 2204512.

(37) Zhuang, R.; Wang, X.; Ma, W.; Wu, Y.; Chen, X.; Tang, L.; Zhu, H.; Liu, J.; Wu, L.; Zhou, W.; Liu, X.; Yang, Y., Highly Sensitive X-Ray Detector Made of Layered Perovskite-Like $(NH_4)_3Bi_2I_9$ Single Crystal with Anisotropic Response. *Nat. Photonics* **2019,** *13* (9), 602-608.

(38) Liu, Y.; Xu, Z.; Yang, Z.; Zhang, Y.; Cui, J.; He, Y.; Ye, H.; Zhao, K.; Sun, H.; Lu, R.; Liu, M.; Kanatzidis, M. G.; Liu, S., Inch-Size 0D-Structured Lead-Free Perovskite Single Crystals for Highly Sensitive Stable X-Ray Imaging. *Matter* **2020,** *3* (1), 180-196.

(39) Xia, M.; Yuan, J. H.; Niu, G.; Du, X.; Yin, L.; Pan, W.; Luo, J.; Li, Z.; Zhao, H.; Xue, K. H.; Miao, X.; Tang, J., Unveiling the Structural Descriptor of $A_3B_2X_9$ Perovskite Derivatives toward X-Ray Detectors with Low Detection Limit and High Stability. *Adv. Funct. Mater.* **2020,** *30* (24), 1910648.

(40) Zheng, X.; Zhao, W.; Wang, P.; Tan, H.; Saidaminov, M. I.; Tie, S.; Chen, L.; Peng, Y.; Long, J.; Zhang, W.-H., Ultrasensitive and Stable X-Ray Detection Using Zero-Dimensional Lead-Free Perovskites. *J. Energy Chem.* **2020,** *49*, 299-306.

(41) Wu, J.; Wang, L.; Feng, A.; Yang, S.; Li, N.; Jiang, X.; Liu, N.; Xie, S.; Guo, X.; Fang, Y.; Chen, Z.; Yang, D.; Tao, X., Self-Powered $FA_{0.55}MA_{0.45}PbI_3$ Single-Crystal Perovskite X-Ray Detectors with High Sensitivity. *Adv. Funct. Mater.* **2021,** *32* (9), 2109149.

(42) Zhang, Y.; Liu, Y.; Xu, Z.; Ye, H.; Yang, Z.; You, J.; Liu, M.; He, Y.; Kanatzidis, M. G.; Liu, S. F., Nucleation-Controlled Growth of Superior Lead-Free Perovskite $Cs_3Bi_2I_9$ Single-Crystals for High-Performance X-Ray Detection. *Nat. Commun.* **2020,** *11* (1), 2304.

(43) Milbrath, B. D.; Peurrung, A. J.; Bliss, M.; Weber, W. J., Radiation Detector

Materials: An Overview. *J. Mater. Res.* **2008,** *23* (10), 2561-2581.

(44) Kasap, S. O., X-Ray Sensitivity of Photoconductors: Application to Stabilized a-Se. *J. Phys. D: Appl. Phys.* **2000,** *33* (21), 2853.

(45) Pan, L.; Shrestha, S.; Taylor, N.; Nie, W.; Cao, L. R., Determination of X-Ray Detection Limit and Applications in Perovskite X-Ray Detectors. *Nat. Commun.* **2021,** *12* (1), 5258.